Development of a new Method for Strain Field Optimized Material Characterization

Maximilian Benz[1], Johannes Irslinger[1], Paul Du Bois[2], Markus Feucht[1], Manfred Bischoff[3]

[1]Daimler AG
[2]Consultant
[3]Institute for Structural Mechanics, University of Stuttgart

1 Introduction

Due to technical progress, cars of the future will consist of even more different materials than they already do today. Especially plastic materials will experience a further increase of importance, as they provide advantages such as a low density and the freedom to shape them unconventionally. In view of this trend, it is essential to improve the quality of predictions derived from corresponding simulations.
Modelling the material in an appropriate way is crucial when simulating a component. While in case of metals plastic deformation happens at a constant volume and therefore is easy to describe, this kind of incompressibility does not apply to plastics. Furthermore, the hardening behavior of these materials is usually significantly more complicated. Therefore, complex mechanical descriptions have to be used for the simulation of plastics, which describe hardening and failure in a multiaxial state of stress. Although those models have been available for some time, it is still cumbersome to calibrate their parameters. In particular, the correct prediction of the strain field, which is the key to characterize material failure e.g. with GISSMO [5], is challenging, as a large number of degrees of freedom have to be adjusted simultaneously.

2 Summary

The objective of the newly developed method is to perform the calibration of the material model ***MAT_SAMP-1** [2, 4] with respect to experimental data without using ansatz functions and reverse engineering. In contrast to previous approaches, the technique allows a predictive simulation not only of the force level, but also of the strain field – including the phase beyond necking (see Figure 1).
Based on local strain data from a material test and postulation of a material model, the stress state is determined by the solution of differential equations. Proceeding from the state of stress, an optimized yield curve can be determined. Moreover, a strain dependent curve for the *plastic Poisson's ratio* v_p (introduced in [2]) is calculated. Both characteristics result from a projection of the current stress and strain state into an equivalent state of pure uniaxial tension.

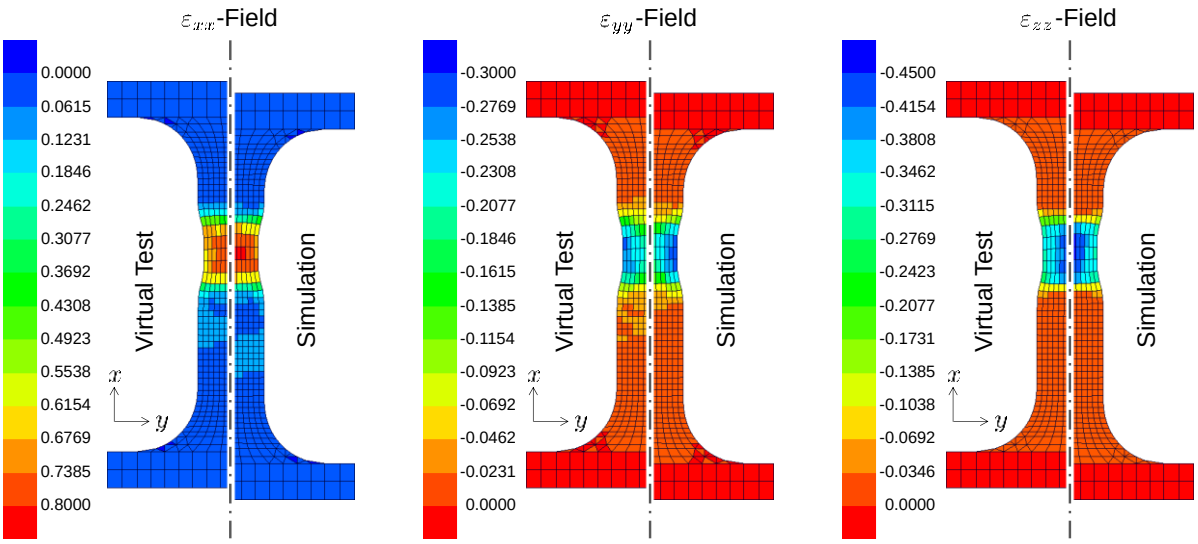

Fig.1: x-, y-, and z-component of the strain tensor in a virtual test and a simulation beyond the necking point

In this early stage, the focus is put on the study of plane stress states in tensile tests, currently without considering rate-dependency of the elastic constants. However, in further developments, generalizations with respect to these simplifications can be implemented. Due to the fact that in case of classical metal plasticity ***MAT_SAMP-1** transforms into ***MAT_024** [4], this model is supported as well.
As a proof of concept in this paper only data sets resulting from virtual tests (simulations) are evaluated. Because in these tests the complete strain and stress field as well as the original yield curve and v_p curve are known, the agreement of the derived parameters can be demonstrated.

3 Mathematical Derivation

The core component of the method is a set of differential equations, which are derived for a point in an isotropic continuum behaving according to ***MAT_SAMP-1**. For this point it is postulated that the global coordinate system (*x*, *y*, *z*) corresponds to the local coordinate system (*1*, *2*, *3*), in which no shear strains are present and that the load is applied in *x*-direction. Furthermore, it is demanded that no rigid-body rotation takes place and that therefore the material derivative of the Cauchy stress tensor is equivalent to the objective Jaumann rate.

3.1 Differential Equations for the Elastic Domain

In the case described above, for an inviscid material, the following three differential equations can be established:

$$\dot{\varepsilon}^{e}_{xx} = \dot{\varepsilon}_{xx} - \dot{\varepsilon}^{p}_{xx} = \frac{1}{E}\dot{\sigma}_{xx} - \frac{\nu}{E}\dot{\sigma}_{yy} - \frac{\nu}{E}\dot{\sigma}_{zz} \tag{1}$$

$$\dot{\varepsilon}^{e}_{yy} = \dot{\varepsilon}_{yy} - \dot{\varepsilon}^{p}_{yy} = \frac{1}{E}\dot{\sigma}_{yy} - \frac{\nu}{E}\dot{\sigma}_{zz} - \frac{\nu}{E}\dot{\sigma}_{xx} \tag{2}$$

$$\dot{\varepsilon}^{e}_{zz} = \dot{\varepsilon}_{zz} - \dot{\varepsilon}^{p}_{zz} = \frac{1}{E}\dot{\sigma}_{zz} - \frac{\nu}{E}\dot{\sigma}_{xx} - \frac{\nu}{E}\dot{\sigma}_{yy} \tag{3}$$

The (elastic) Poisson's ratio *v* is constant and must be determined by evaluation of a uniaxial state of stress:

$$\nu = -\frac{\dot{\varepsilon}^{e}_{yy}}{\dot{\varepsilon}^{e}_{xx}} = -\frac{\dot{\varepsilon}^{e}_{zz}}{\dot{\varepsilon}^{e}_{xx}} \tag{4}$$

In a plane state of stress the stress component in *z*-direction and its time derivative vanish and the system (1) – (3) reduces to:

$$\dot{\varepsilon}^{e}_{xx} = \dot{\varepsilon}_{xx} - \dot{\varepsilon}^{p}_{xx} = \frac{1}{E}\dot{\sigma}_{xx} - \frac{\nu}{E}\dot{\sigma}_{yy} \tag{5}$$

$$\dot{\varepsilon}^{e}_{yy} = \dot{\varepsilon}_{yy} - \dot{\varepsilon}^{p}_{yy} = \frac{1}{E}\dot{\sigma}_{yy} - \frac{\nu}{E}\dot{\sigma}_{xx} \tag{6}$$

$$\dot{\varepsilon}^{e}_{zz} = \dot{\varepsilon}_{zz} - \dot{\varepsilon}^{p}_{zz} = -\frac{\nu}{E}\dot{\sigma}_{xx} - \frac{\nu}{E}\dot{\sigma}_{yy} \tag{7}$$

Introduction of the stress ratio

$$a = \frac{\sigma_{yy}}{\sigma_{xx}} \quad \text{with} \quad \sigma_{xx} \neq 0 \tag{8}$$

yields the following system, which is valid for both, the elastic and the elastoplastic domain:

$$\dot{\varepsilon}_{xx}^{\ e} = \dot{\varepsilon}_{xx} - \dot{\varepsilon}_{xx}^{\ p} = \frac{1}{E}\dot{\sigma}_{xx} - \frac{\nu}{E}\dot{a}\sigma_{xx} - \frac{\nu}{E}a\dot{\sigma}_{xx} \tag{9}$$

$$\dot{\varepsilon}_{yy}^{\ e} = \dot{\varepsilon}_{yy} - \dot{\varepsilon}_{yy}^{\ p} = \frac{1}{E}\dot{a}\sigma_{xx} + \frac{1}{E}a\dot{\sigma}_{xx} - \frac{\nu}{E}\dot{\sigma}_{xx} \tag{10}$$

$$\dot{\varepsilon}_{zz}^{\ e} = \dot{\varepsilon}_{zz} - \dot{\varepsilon}_{zz}^{\ p} = -\frac{\nu}{E}\dot{\sigma}_{xx} - \frac{\nu}{E}\dot{a}\sigma_{xx} - \frac{\nu}{E}a\dot{\sigma}_{xx} \tag{11}$$

As in the elastic domain the plastic strain rates disappear equations (9) – (11) become:

$$\dot{\varepsilon}_{xx}^{\ e} = \dot{\varepsilon}_{xx} = \frac{1}{E}\dot{\sigma}_{xx} - \frac{\nu}{E}\dot{a}\sigma_{xx} - \frac{\nu}{E}a\dot{\sigma}_{xx} \tag{12}$$

$$\dot{\varepsilon}_{yy}^{\ e} = \dot{\varepsilon}_{yy} = \frac{1}{E}\dot{a}\sigma_{xx} + \frac{1}{E}a\dot{\sigma}_{xx} - \frac{\nu}{E}\dot{\sigma}_{xx} \tag{13}$$

$$\dot{\varepsilon}_{zz}^{\ e} = \dot{\varepsilon}_{zz} = -\frac{\nu}{E}\dot{\sigma}_{xx} - \frac{\nu}{E}\dot{a}\sigma_{xx} - \frac{\nu}{E}a\dot{\sigma}_{xx} \tag{14}$$

It can be seen, that the stress ratio *a* is the only unknown in this system of linear ODEs. To deal with this overdetermination any of the three equations can be chosen or an appropriate method to solve several equations simultaneously must be applied. In case of perfectly consistent input data, free of measurement errors, all three ODEs give the same result.

3.2 Differential Equations for the Elastoplastic Domain

Besides the specification of a yield curve ***MAT_SAMP-1** requires the declaration of a plastic Poisson's ratio v_p, which is typically not constant, but strain dependent. Analogously to the (elastic) Poisson's ratio *v* (see equation (4)) [2] states for a uniaxial state of stress:

$$\nu_p = -\frac{\dot{\varepsilon}_{yy}^{\ p}}{\dot{\varepsilon}_{xx}^{\ p}} = -\frac{\dot{\varepsilon}_{zz}^{\ p}}{\dot{\varepsilon}_{xx}^{\ p}} \tag{15}$$

By default ***MAT_SAMP-1** uses a non-associated flow rule with a plastic potential *g*:

$$g = \sqrt{\sigma_{vm}^2 + \alpha p^2} \tag{16}$$

In this equation, α is a material characteristic that is directly dependent on the value of v_p in the projection of the current stress and strain state into an equivalent state of pure uniaxial tension [2]:

$$\alpha = \frac{9}{2}\frac{1-2\nu_p}{1+\nu_p} \quad \leftrightarrow \quad \nu_p = \frac{9-2\alpha}{18+2\alpha} \tag{17}$$

From equation (17) it follows that the following holds for classical metal plasticity:

$$\alpha = 0 \quad \leftrightarrow \quad \nu_p = 0.5 = \text{const} \tag{18}$$

In this case, the plastic potential *g* transforms into the von Mises yield criterion as implemented in ***MAT_024.**

For a non-associated flow rule, the following relation between the tensor of plastic strain rates $\partial(\boldsymbol{\varepsilon}^p)/\partial t$, the plastic multiplier λ, the plastic potential g and the stress tensor $\boldsymbol{\sigma}$ can be stated:

$$\dot{\boldsymbol{\varepsilon}}^{\mathbf{P}} = \dot{\lambda}\frac{\partial g}{\partial \boldsymbol{\sigma}} \tag{19}$$

The von Mises stress σ_{vm} in (16) depends on the second invariant of the stress deviator tensor $\mathbf{s}$:

$$\sigma_{vm} = \sqrt{3J_2} = \sqrt{\frac{3}{2}\mathbf{s} : \mathbf{s}} \tag{20}$$

with:

$$\mathbf{s} = \boldsymbol{\sigma} + p\boldsymbol{\delta} \tag{21}$$

Furthermore, the hydrostatic pressure p in (16) and (21) follows from the first invariant of the stress tensor:

$$p = -\frac{I_1}{3} = -\frac{\mathrm{tr}\,(\boldsymbol{\sigma})}{3} \tag{22}$$

Inserting (20) – (22) in (16) and then evaluating (19) yields:

$$\dot{\boldsymbol{\varepsilon}}^{\mathbf{P}} = \dot{\lambda}\frac{\partial g}{\partial \boldsymbol{\sigma}} = \frac{3\dot{\lambda}}{2g}\left(\mathbf{s} - \frac{2}{9}\alpha p\boldsymbol{\delta}\right) \tag{23}$$

From this relation, the following two equations can be derived:

$$\frac{\dot{\varepsilon}_{yy}^{\,p}}{\dot{\varepsilon}_{xx}^{\,p}} = \frac{2a - 1 + 2\beta\,(1+a)}{2 - a + 2\beta\,(1+a)} \tag{24}$$

$$\frac{\dot{\varepsilon}_{zz}^{\,p}}{\dot{\varepsilon}_{xx}^{\,p}} = \frac{-a - 1 + 2\beta\,(1+a)}{2 - a + 2\beta\,(1+a)} \tag{25}$$

The factor β was introduced for the sake of brevity and is defined by:

$$\beta = \frac{\alpha}{9} \tag{26}$$

By combining equations (24) and (25) with the general applicable ones from (9) – (11), a system of five differential equations with five unknowns (a, $\beta(\nu_p)$, $\partial(\varepsilon_{xx}^p)/\partial t$, $\partial(\varepsilon_{yy}^p)/\partial t$, $\partial(\varepsilon_{zz}^p)/\partial t$) can be established:

$$\dot{\varepsilon}_{xx} - \dot{\varepsilon}_{xx}^{\,p} = \frac{1}{E}\dot{\sigma}_{xx} - \frac{\nu}{E}\dot{a}\sigma_{xx} - \frac{\nu}{E}a\dot{\sigma}_{xx} \tag{9}$$

$$\dot{\varepsilon}_{yy} - \dot{\varepsilon}_{yy}^{\,p} = \frac{1}{E}\dot{a}\sigma_{xx} + \frac{1}{E}a\dot{\sigma}_{xx} - \frac{\nu}{E}\dot{\sigma}_{xx} \tag{10}$$

$$\dot{\varepsilon}_{zz} - \dot{\varepsilon}_{zz}^{\,p} = -\frac{\nu}{E}\dot{\sigma}_{xx} - \frac{\nu}{E}\dot{a}\sigma_{xx} - \frac{\nu}{E}a\dot{\sigma}_{xx} \tag{11}$$

$$\frac{\dot{\varepsilon}_{yy}^{\,p}}{\dot{\varepsilon}_{xx}^{\,p}} = \frac{2a - 1 + 2\beta\,(1+a)}{2 - a + 2\beta\,(1+a)} \tag{24}$$

$$\frac{\dot{\varepsilon}_{zz}^{p}}{\dot{\varepsilon}_{xx}^{p}} = \frac{-a - 1 + 2\beta\,(1 + a)}{2 - a + 2\beta\,(1 + a)} \tag{25}$$

If v_p is unknown, which is in general the case, the equations can be combined to get a single linear ODE:

$$\left[-\frac{1}{E}\sigma_{xx} - \frac{\nu}{E}\sigma_{xx}\right]\dot{a} + \left[\dot{\varepsilon}_{zz} - \dot{\varepsilon}_{xx}\right]a + \dot{\varepsilon}_{yy} - \dot{\varepsilon}_{zz} = 0 \tag{27}$$

If v_p is specified, $\partial(\varepsilon_{zz})/\partial t$ and $\partial(\varepsilon_{zz}^{p})/\partial t$ are coupled directly to this quantity by ignoring equations (11) and (25). Consequently, a non-linear ODE can be established:

$$\begin{aligned}
&\left(\left[(2\nu - 1)\,\frac{\sigma_{xx}}{E} + 2\beta\frac{1+\nu}{E}\sigma_{xx}\right]a + \left[(2 - \nu)\,\frac{\sigma_{xx}}{E} + 2\beta\frac{1+\nu}{E}\sigma_{xx}\right]\right)\dot{a} \\
&\left(\left[(2\nu - 1)\,\frac{\dot{\sigma}_{xx}}{E} + 2\beta\frac{1+\nu}{E}\dot{\sigma}_{xx}\right]a + \left[2\dot{\varepsilon}_{xx} + \dot{\varepsilon}_{yy} + 2\beta\,(\dot{\varepsilon}_{xx} - \dot{\varepsilon}_{yy})\right]\right)a \\
&-\dot{\varepsilon}_{xx} - 2\dot{\varepsilon}_{yy} - (2\nu - 1)\,\frac{\dot{\sigma}_{xx}}{E} + 2\beta\left(\dot{\varepsilon}_{xx} - \dot{\varepsilon}_{yy} - \frac{1+\nu}{E}\dot{\sigma}_{xx}\right) = 0
\end{aligned} \tag{28}$$

This approach is justified by the fact that the measurement of ε_{zz} contains the largest uncertainty.

3.3 Yield Curve and Curve for Plastic Poisson's Ratio

To solve the differential equations derived in Sections 3.1 and 3.2, numerical solution methods are applied. After the stress ratio a is available, the hydrostatic pressure p and the von Mises stress σ_{vm} follows immediately. The time derivative of the stress ratio is obtained by using difference quotients. Afterwards, the components of the plastic strain rate tensor can be determined by evaluating equations (9) – (11). Furthermore, by using (17) and (26) the plastic Poisson's ratio v_p follows from (24) or (25).
So far, all of these quantities are functions of time, however, as abscissa for yield curve and v_p curve ***MAT_SAMP-1** expects a *uniaxial plastic strain* ε^{pct} (introduced in [2]), which is defined as a projection of the current strain state into an equivalent state of pure uniaxial tension. Following the documentation in [2], the variation of the rate of this quantity over time is established. After numerical integration, a yield curve and a v_p curve are obtained by eliminating time from the functional relations.

3.4 Validation with a Single-Element Test

To validate the described method, a virtual test with a single fully integrated finite shell element (**ELFORM=16**) is performed. As this formulation complies with the 5-parameter Reissner-Mindlin model, strains $\varepsilon_{zz} \neq 0$ are not supported in its original specification. However, by activating the option **ISTUPD=1**, a thickness change based on the material model and driven by the membrane strains is incorporated – also when calculating the nodal forces [3].
The element and its boundary conditions are sketched in Figure 2 and as indicated there, applied displacements in x- and y-direction enforce a plane biaxial state of stress. The magnitude of these loads is arbitrary and irrelevant for the following discussion. As material model ***MAT_SAMP-1** is chosen and as yield curve and v_p curve typical shapes for a thermoplastic are stated.

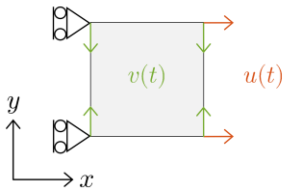

Fig.2: Validation with a single-element test

After executing the simulation, the stress in *x*-direction σ_{xx} as well as the strains ε_{xx}, ε_{yy} and ε_{zz} over time are evaluated and subsequently used as input for the developed algorithm. As it can be seen in Figure 3, apart from presumably numerical disturbances, the calculated yield curve, the v_p curve and the stress ratio agree with the ones from the virtual test. This is a strong indication for the proper functioning of the method.

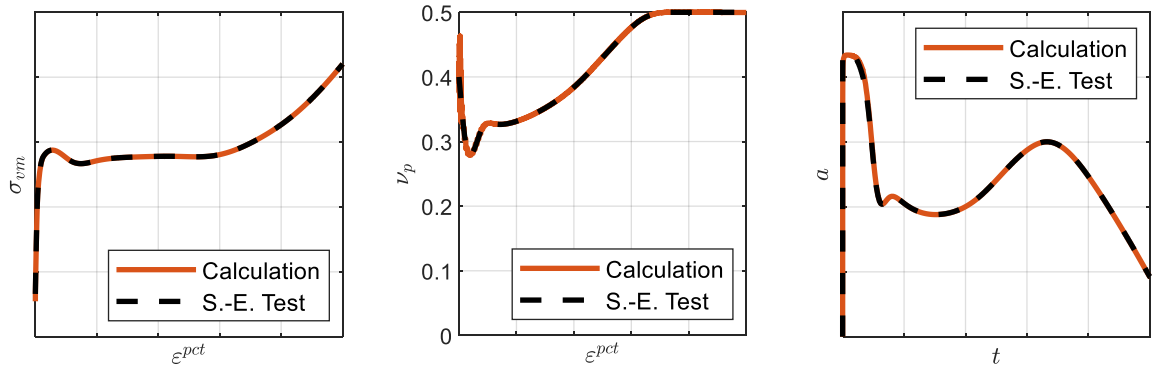

Fig.3: From left to right: Calculated yield curve, v_p curve and stress ratio – each with its counterpart from the single-element test

4 General Applicability to Tensile Specimen

The derived differential equations can be used for analyzing the deformation behavior of thin tensile specimens. In this case, the stress and strain state in the center of the necking area must be gathered, as at this point the shear strains ε_{xy}, ε_{xz} and ε_{yz} are zero due to symmetry. Furthermore, a sufficiently small thickness of the specimen leads to a stress state close to plane stress. If necking occurs halfway between the clamping areas, then the described location coincides with the origin of a centrally positioned coordinate system (see Figure 4). In the following, the above statement is verified by executing and evaluating virtual tensile tests.

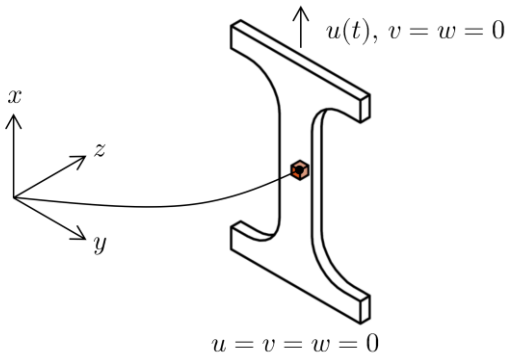

Fig.4: Tensile specimen with clamping areas partly blanked out – of particular interest is the stress and strain state in the center of the necking area

4.1 Tensile Test of a Typical Steel

First, a **`*MAT_024`** model of a typical steel is investigated. In this case, the value of the plastic Poisson's ratio is 0.5. As shown in Figure 5, the developed algorithm correctly reproduces both the yield curve and the v_p curve. After a simulation with the newly calculated yield curve (in **`*MAT_024`** v_p = 0.5 is fixed), it becomes clear that the reproduction of the force level is also given.
Figure 6 depicts the *x*-, *y*-, and *z*-component of the strain tensor in the virtual test and the simulation beyond the necking point. The correct reproduction of the strain field at this displacement is exemplary for the whole study.

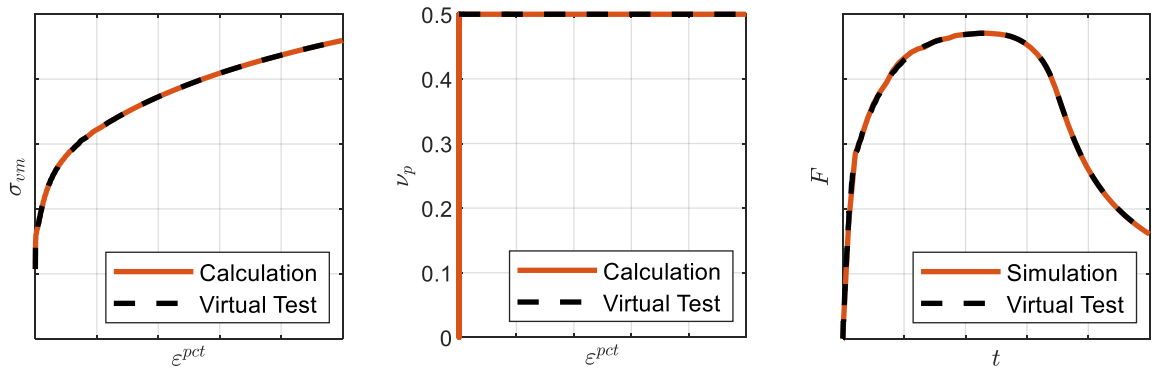

Fig.5: From left to right: Calculated yield curve, calculated v_p curve and force level from a simulation – each with its counterpart from the virtual test

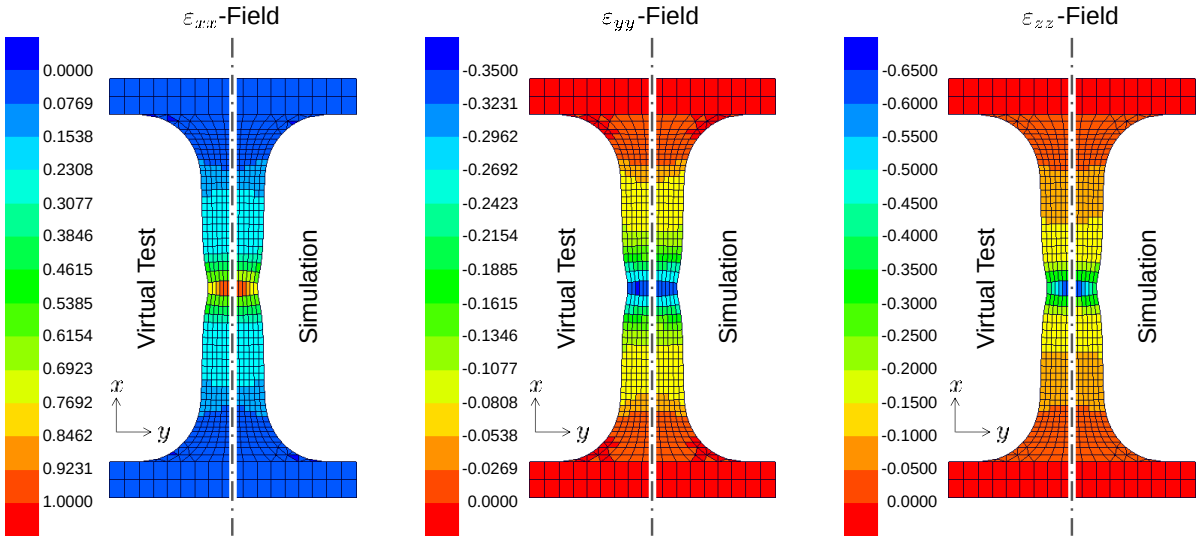

Fig.6: x-, y-, and z-component of the strain tensor in the virtual test and a simulation beyond the necking point (input data from Figure 5)

4.2 Tensile Test of a Typical Thermoplastic

In the next step of verification, the **`*MAT_SAMP-1`** material model from Section 3.4 is examined. As it can be seen in Figure 7, also in this case the algorithm predicts the yield curve and the v_p curve very well. However, the v_p curve shows strong oscillations at its beginning, which must be removed before using it for a simulation. An explanation for this characteristic is given later on. In the following, the v_p curve is smoothed and the start value is set to 0.4, which corresponds to the value of the (elastic) Poisson's ratio of the material. Next, a new yield curve is calculated with the smoothed v_p curve given. By doing so, compatibility between both data sets is guaranteed. A simulation with the newly calculated curves proves the given reproduction of the force level.
Figure 8 shows the *x*-, *y*-, and *z*-component of the strain tensor in the virtual test and the simulation beyond the necking point. Although the location of necking is not exactly the same, the correct reproduction of its shape and the strain field at this displacement are exemplary for the whole study.

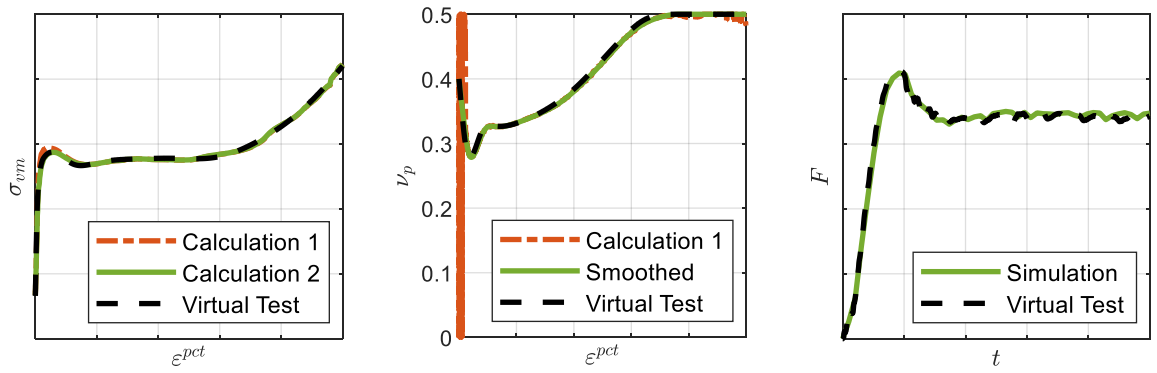

Fig.7: From left to right: Calculated yield curves, calculated and smoothed v_p curve and force level from a simulation – each with its counterpart from the virtual test

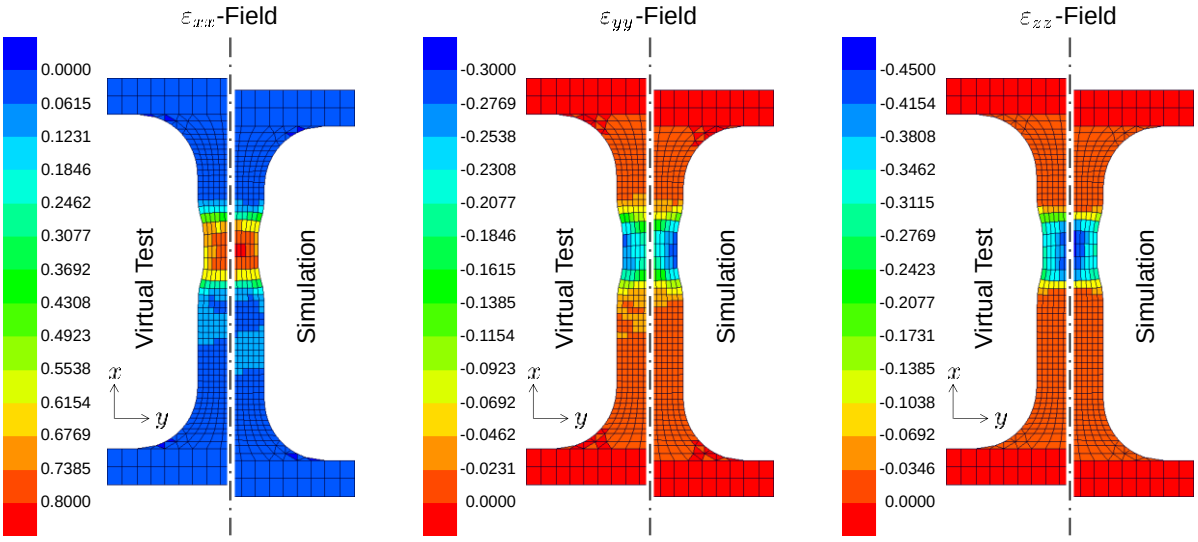

Fig.8: x-, y-, and z-component of the strain tensor in the virtual test and a simulation beyond the necking point (input data from Figure 7)

As it can be seen in the right plot of Figure 7, the force level over time is not smooth. The reason for this is that the corresponding yield curve of the thermoplastic is not monotonically increasing. As a consequence, rows of elements subsequently soften and harden. On the left side of Figure 9, $\partial(\varepsilon_{xx})/\partial t$ of the central shell elements parallel to the *x*-axis at $y = 0$ is plotted over *t* in a shared diagram.

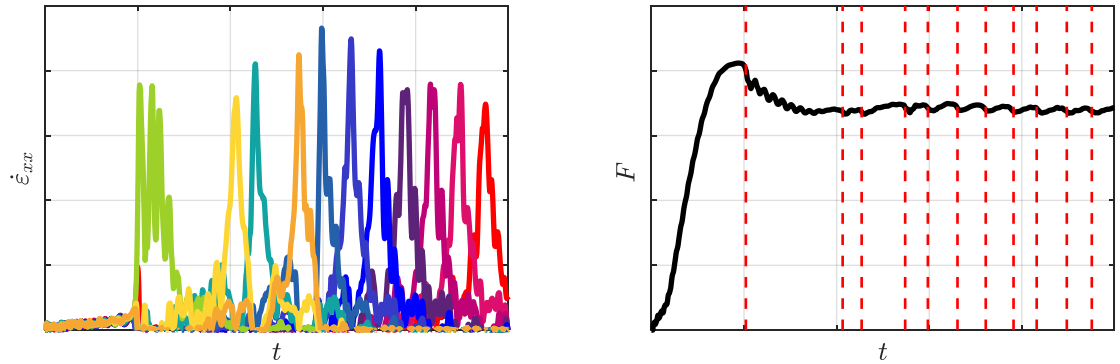

Fig.9: Left: $\partial(\varepsilon_{xx})/\partial t$ vs. t of the central shell elements parallel to the x-axis at y = 0; right: global F vs. t plot – positions of vertical lines correspond to the maxima of those $\partial(\varepsilon_{xx})/\partial t$ curves with peaks

On the right side of Figure 9, the global *F* vs. *t* plot of the original simulation is shown. In this diagram, the positions of the vertical red lines correspond to the maxima of those $\partial(\varepsilon_{xx})/\partial t$ curves with values larger than a specified threshold. It can be clearly seen, that those lines divide the plot in recurring patterns, emerging from softening and hardening of individual elements and element rows, respectively. The described effect is not only numerical, but in fact has its origin in nature. It is typical for thermoplastics and known in literature as so-called *telescope effect* [1].
It is evident that the described behavior of the material does effect the local quantities such as elementwise strains and stresses as well. Consequently, especially σ_{xx} at the element in the center of the necking area is not smooth over time. As the algorithm needs the derivative of this quantity with respect to time, it is inevitable to eliminate the disturbances in this curve. Smoothing, however, is another potential source of errors and this might be the reason, why the v_p curve in Figure 7 shows strong oscillations at its beginning.

5 Challenges in Application to Real Tensile Tests

5.1 Necessity of an Iterative Approach

In a real tensile test the stress distribution in the specimen cannot be measured. For this reason, the *x*-component of the stress tensor in the center of the necking area σ_{xx} is approximated by:

$$\overline{\sigma}_{xx} = \frac{F}{A} \tag{29}$$

In this context, *F* is the force level and *A* is the time-dependent cross section of the specimen in the necking plane – a plane parallel to the *y*-*z*-plane. As long as no localization is observed in the tensile test, it holds:

$$\overline{\sigma}_{xx} = \sigma_{xx} \tag{30}$$

However, as soon as necking starts, the stress distribution over the cross section is no longer constant and the integral approximation deviates from the demanded value. For the investigated cases from Section 4, the discrepancy is depicted in Figure 10.

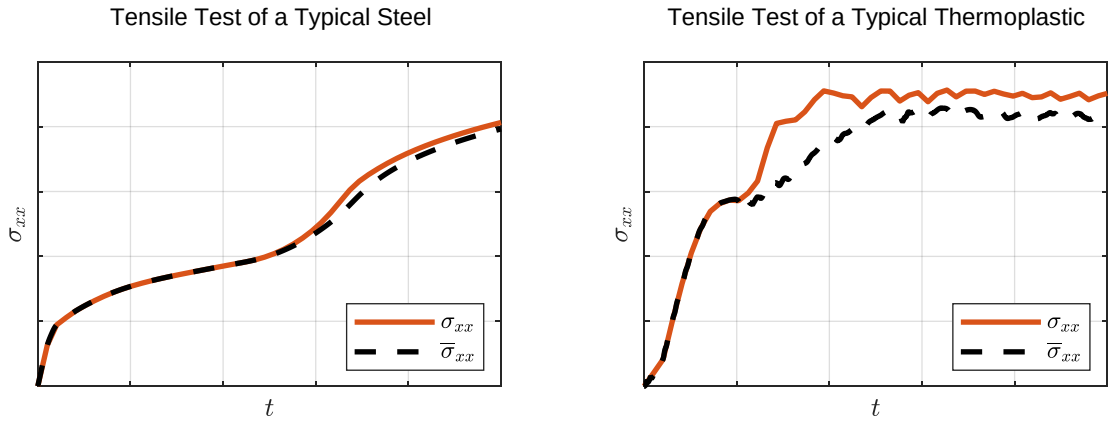

Fig.10: x-components of the stress tensor in the central elements and their integral approximations; left: virtual test of steel from section 4.1; right: virtual test of thermoplastic from section 4.2

It turns out that the deviations in σ_{xx} have a large impact on the calculated yield curve, but are negligible with respect to the resulting v_p curve. Consequently, an iterative approach for executing and evaluating a real tensile test is established. The underlying algorithm is as follows:

1. Execution of tensile test with thin specimen, record of the displacement field with three-dimensional image correlation techniques

2. Evaluation of the strain state in the center of the necking area, determination of an integral approximation for the *x*-component of the stress tensor at this point
3. Calculation of yield curve and v_p curve
4. Execution of a simulation of the tensile test with these material characteristics – the applied displacement vs. time must correspond to the one from the original test
5. If the yield curve contains errors due to the approximation of σ_{xx}, the force level of the simulation F_{iter} will deviate from the original level F → Calculation of a correction function for σ_{xx} based on the ratio F/F_{iter}
6. Correction of σ_{xx} in the phase beyond necking and begin of an iterative loop starting with step 3 – the v_p curve can either be newly calculated as well or remain unchanged
7. Convergence is reached if the maximum error in force level is smaller than a specified threshold ϵ: $\max(|[F(t^n)-F_{iter}(t^n)]/F(t^n)|)<\epsilon$ with $0 \le n \le n_{max}$

5.2 Tensile Test of a Typical Steel

The iterative approach described above is first demonstrated for the **`*MAT_024`** model of a typical steel from Section 4.1. As depicted in Figure 11, after 16 iterations (red curves) the force level from the simulation deviates less than 1% from the one of the virtual test. In this case, agreement can also be observed in both, σ_{xx} and the yield curve.
Figure 12 shows the *x*-, *y*-, and *z*-component of the strain tensor in the virtual test and the 16th repeated simulation beyond the necking point. The correct reproduction of the strain field at this displacement is exemplary for the whole study.

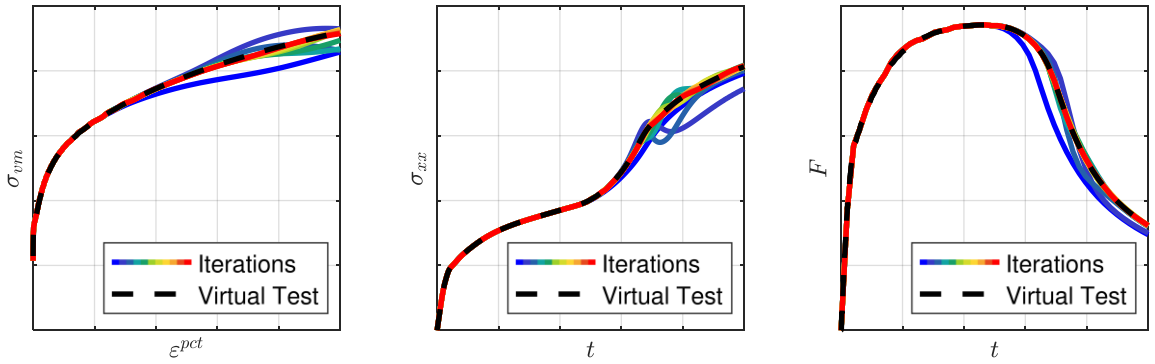

Fig.11: From left to right: Iterated yield curves, corresponding σ_{xx} and force levels from simulations – all with their counterpart from the virtual test

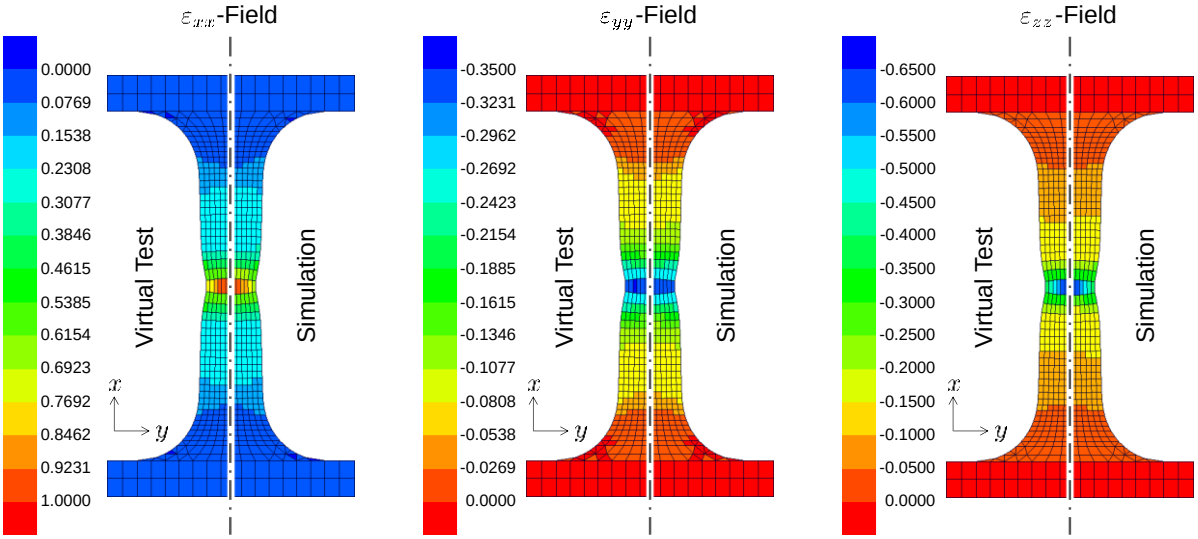

Fig.12: x-, y-, and z-component of the strain tensor in the virtual test and a simulation beyond the necking point (input data from Figure 11)

5.3 Tensile Test of a Typical Thermoplastic

Next, the ***MAT_SAMP-1** material model of a typical thermoplastic from Section 3.4 and 4.2 is examined. Due to the perturbing influence of softening and hardening patterns in the force level, both the convergence criterion and the correction function for σ_{xx} are based on smoothed curves. In the present case, an acceptably smooth force level was achieved by fitting a polynomial of higher order, however, in further development, this subject must and will be further addressed.
After 10 iterations the smoothed force level from the simulation deviates less than 1% from the one of the virtual test. Consequently, also the original curves in Figure 13 almost coincide. The original yield curve is approximated in a good manner. However, larger deviations can be observed in the plot of σ_{xx}. Here, artificial oscillations coming from the polynomial of higher order are evident.
Despite the shape of σ_{xx} in the final iteration, the calculated yield curve leads to a good agreement of the strain field in the virtual test and the 10th simulation. This can be seen in Figure 14. Again, the correct reproduction at this displacement beyond the necking point is exemplary for the whole study.

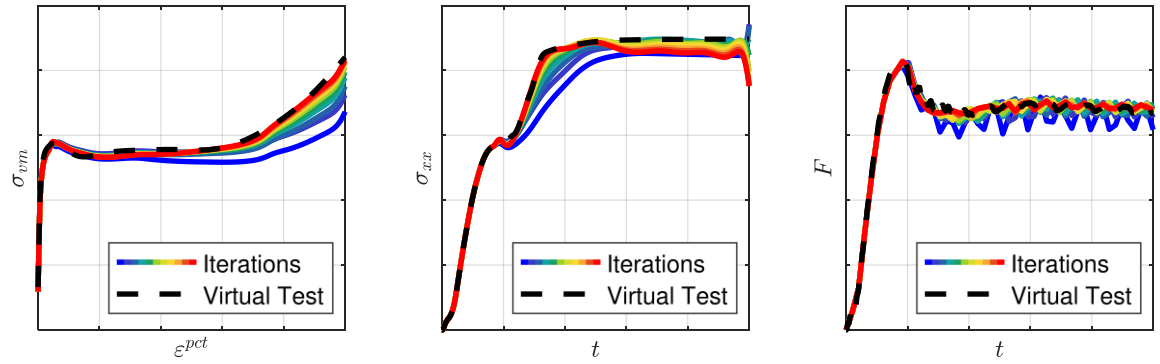

Fig.13: From left to right: Iterated yield curves, corresponding σ_{xx} and force levels from simulations – all with their counterpart from the virtual test

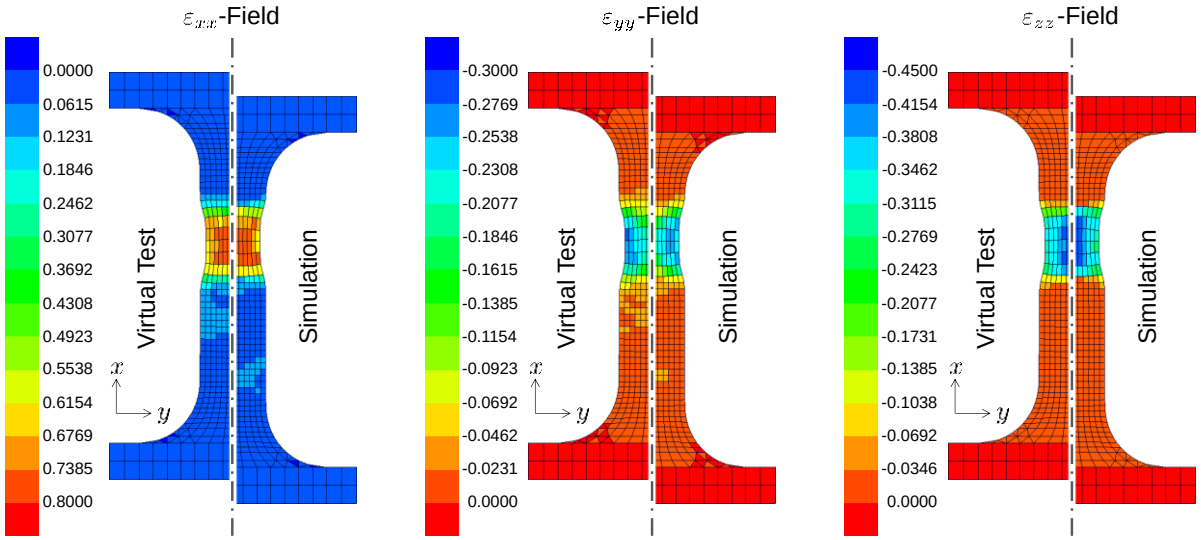

Fig.14: x-, y-, and z-component of the strain tensor in the virtual test and a simulation beyond the necking point (input data from Figure 13)

6 Conclusion and Outlook

It was shown, that in case of ideal tensile test data sets, the newly developed method is capable of reproducing the yield curve and v_p curve of the used material models ***MAT_SAMP-1** and ***MAT_024**. Simulations with the calculated input do not only reproduce the force level, but also the original strain field of the virtual tests – including the phase beyond necking. In hardware tests, the stress distribution in the tensile specimen cannot be measured. For this reason, an iterative approach was established, which is capable of dealing with an integral approximation of σ_{xx} in the center of the necking area rather than the exact value.
As mentioned in Section 5.1, the evaluation of real tensile tests requires a record of the displacement field with three-dimensional image correlation techniques. Although the results of the first hardware tests are promising, they show that implementation of suitable and stable smoothing algorithms is the key for the further development. Naturally, the data sets coming from real tensile tests are superimposed with noise. However, as the method requires the time derivatives of strains and stress, the impact of these disturbances is even increased. The importance of smoothing algorithms is also present in the iterative approach stated above, because the calculation of an internal correction function for σ_{xx} requires smooth force levels.

7 Literature

[1] Elias, H.-G.: “Polymere: Von Monomeren und Makromolekülen zu Werkstoffen. Eine Einführung”, UTB für Wissenschaft Makromolekulare Chemie, Polymerwissenschaften, Hüthig und Wepf Verlag, Zug – Heidelberg – Oxford, 1996.

[2] Kolling, S.; Haufe, A.; Feucht, M.; Du Bois, P. A.: “SAMP-1: A Semi-Analytical Model for the Simulation of Polymers”, Keynote presented at Deutsches LS-DYNA Forum, Bamberg, 2005, pp. A–II–27 - A–II–52.

[3] LSTC: “LS-DYNA Keyword User’s Manual – Volume I – LS-DYNA R11”, Livermore, 2018.

[4] LSTC: “LS-DYNA Keyword User’s Manual – Volume II: Material Models – LS-DYNA R11”, Livermore, 2018.

[5] Neukamm, F.: “Lokalisierung und Versagen von Blechstrukturen”, Doctoral dissertation, Institute for Structural Mechanics, University of Stuttgart, Stuttgart, 2018.